Hall R C (Ed), 1997. Evaluating modelling uncertainty - Project EMU Final Report. WS Atkins Report WSA/AM5017/R7
Chapter 4

4 WIND TUNNEL EXPERIMENTS

4.1 Experimental Facilities

The EnFlo wind tunnel at the University of Surrey (see Figure 4.1a) was used for all the experimental studies. It is an open return tunnel with a 20 m long working section which is 3.5 by 1.5 m in cross-section. It has the unique capability amongst U. K. environmental facilities of generating stable, unstable and neutral boundary layer conditions. The operating speed range is from about 0.5 to 4.5 ms^{-1}, this being determined by the constraints involved with the simulation of buoyant flows.

Operation in the stratified mode, illustrated by Figure 4.1b, involves detailed control of the temperature distribution in the flow entering the working section and of the heating and cooling of the tunnel surfaces, principally the floor. The former is provided by an inlet heater section comprising 15 separate, 100 mm deep heating zones, each containing heater elements, with an overall 400 kW power rating. The temperature of the flow leaving each zone is independently controlled and monitored. Stable boundary layers are established by using the inlet heater to produce a profiled initial temperature distribution, allowing this to develop within a simulated boundary layer and then cooling sections of the tunnel floor. A chilled water system is used for this latter purpose. A heat exchanger is located between the working section and the fans to return the flow temperature to ambient conditions. A careful balance must be struck between the flow and the heating and cooling conditions in order to provide the desired boundary layer characteristics; e.g. equivalent to a moderately stable atmosphere. This inevitably implies operating the tunnel at low air speeds, typically about 1 ms^{-1}, which in turn implies rather long experimental run times.

The tunnel is fitted with a computer controlled, three dimensional traverse mechanism so that extensive programmes of work, including instrumentation calibrations, can be executed automatically. Thorough condition monitoring (including flow speed and temperature distributions) is included in the rig-running software. This is essential for establishing experimental quality and is used together with other systems to permit safe, unmanned operation.

For EMU Project work, the traverse system carried either single or crossed hot-wire probes for velocity measurements or arrays of flow sampling tubes for concentration measurements. Hot wire anemometry is a well established and extensively used technique - the systems used in the EnFlo Laboratory are described in Heist et al (1995). Anemometers are calibrated against a standard reference device, a propeller anemometer with valid manufacturer's calibration. Heist et al also cover the gas sampling system, but some comment is warranted here as this is by no means such a

widely used technique (largely reflecting the relatively small number of dispersion studies undertaken vis-à-vis flow studies).

Concentration measurement is based on flame ionisation detector instrumentation with a simple hydrocarbon used as the trace gas. The detectors are straightforward to calibrate and use and have a very wide, linear response to hydrocarbon concentration. At EnFlo we use ethylene as the tracer (its molecular weight is almost exactly that of air) and pre-mix it with a carrier gas to obtain appropriate densities for the gases emitted during experiments.

Experiments begin with the release of the gas mixture at a predetermined rate, monitored and controlled by a thermal mass flow meter based system. The meters are calibrated against a standard displacement volume flow meter. Gas samples are extracted from up to 16 points within the wind tunnel and stored for subsequent analysis. Gas sampling times are selected to ensure overall repeatability to within 10%. Additional samples are taken and stored for background level determination and calibration purposes. Both the calibration and emission gases are obtained in pre-mixed form with certificates of composition.

The discharge is then stopped and the stored samples passed sequentially to the flame ionisation detector which determines the total amount of hydrocarbon within each. The detector's output is converted to an ethylene concentration (by volume) and corrected for the background level. Finally, the set of concentrations, C, are non-dimensionalised as $C.U_h.h^2/Q$, where U_h is the roof level wind speed, h the building height and Q the ethylene emission rate. These results, along with the experimental conditions, are saved in a uniquely named simple text file.

4.2 Simulation Procedures

The model, the emission and the approach flow make up the three elements of the simulations. We look at each in turn below.

4.2.2 The Model

Specification of building dimensions and orientations, together with source size and location, for all the test cases is set out in Section 3. Here we simply add a few comments about the wind tunnel models. Table 4.1 lists the main model features and the scale chosen for the each of the wind tunnel simulations.

Distinguishing between the models used for the Series A and B cases from those used for Series C simplifies the description. Series A and B models were manufactured from perspex or wood, with sharp edges to minimise Reynolds number effects. The L-shaped emitting building was hollow and was fed with source gas from an over-head supply line. The internal volume acted as a settling chamber. The sources themselves were all sharp edged and in the case of the doorway emission, Series A Case 1, covered

by a fine wire mesh to improve flow uniformity. The model buildings were mounted directly on the floor of the wind tunnel.

Test Case Series	Case No.	Scale	Model Features
A	1	1/200	L-shaped building wind direction 0˚
A	2	1/133	L-shaped building wind direction 45˚
B	3	1/200	L-shaped building plus slab-shaped building
B	5	1/133	L-shaped building wind direction 45˚
C	1	1/250	Industrial site, wind direction 0˚

Table 4.1
Wind Tunnel Model Summary

The Series C model involved site terrain as well as buildings. The terrain model was manufactured from expanded polyurethane foam. A terrain height and building dimension data base was generated from site drawings and U. K. Ordnance Survey digital data on a regular 10 m grid. A matching aerodynamic roughness length data base was also created; four roughness categories were used as detailed in Table 4.2. The resulting data files were issued to all partners, providing a common base for constructing physical and numerical site models. Robins (1996) describes the primary data sources and their subsequent manipulation to form the final data sets.

Surface Category	Condition	Roughness Length mm at full scale
1	sea	75
2	open land	75
3	villages & towns	200 to 300
4	industrial sites (with main buildings modelled explicitly)	100

Table 4.2
Surface Categories and Roughness Lengths

4.2.3 Emission Simulation

Emissions are specified by the source geometry, characterised by the area A, and the emission speed and density, V_S and ρ_S. This implies that the following group of parameters must be conserved in the wind tunnel simulations: ρ_S/ρ, V_S/U, $g/U.L$, A/L^2, where ρ is the ambient density, U a reference wind speed and L a reference length scale

(e.g. the building height). This leads to relations between model, suffix m, and full scale conditions, namely:

$$U_m/U = \varepsilon^{1/2}$$
$$(V_S/U)_m = V_S/U$$
$$(\rho_S/\rho)_m = \rho_S/\rho$$
$$(A/L^2)_m = A/L^2$$

where ε is the scale ratio, L_m/L. Control of the required wind tunnel speed can only be exercised through the choice of the geometrical scale. However, this is limited by implications regarding boundary layer depth (as discussed in the following section) and the extent of the terrain which needs to be modelled. For example, we might chose to work at a model scale of 1/200 (the 10 m tall building reducing to 50 mm at model scale) for which we have $U_m/U=1/14$. This is very restrictive as it implies very low wind tunnel operating speeds, too low for reliable control even at these rather modest scales.

Robins (1980) and Snyder (1981) have investigated this issue and concluded that a reduced set of scaling criteria can be successfully defined based on conservation of geometrical scales (such as A/L^2), and the non-dimensional source momentum and buoyancy fluxes, F_M* and F_B*:

$$F_B^* = F_B/U^3.L$$
$$F_M^* = F_M/U^2.L^2$$

where F_M and F_B are the fluxes:

$$F_M = \alpha.V_S.Q$$
$$F_B = g'.Q$$

with Q the volume emission rate ($V_S.A$), α the density ratio (ρ_S/ρ) and g' the modified gravitational acceleration; $g'=g.(1-\alpha)$. The adequacy of this approach has been proved by application to power station stack emissions (Robins, 1980; Obasaju and Robins, 1997) and building effected buoyant releases (Macdonald et al, 1988).

The relationships between model and full scale wind and emission speeds can be written:

$$U_m/U = \varepsilon^{1/2}.\{[(1-\alpha_m)/(1-\alpha)].(\alpha/\alpha_m)^{1/2}\}^{1/2}$$
$$(V_S/U)_m = (\alpha/\alpha_m)^{1/2}.(V_S/U)$$

leaving the density ratio, α, as a free parameter. We immediately see the benefit of setting $\alpha_m<\alpha$. Simulations were undertaken at scales of 1/133, 1/200 and 1/250, the choice resting primarily on the available density distortion, α_m/α, and the implied wind tunnel operating speed. The aim was to work with a tunnel reference speed (i.e. the

speed at the edge of the boundary layer) of $1ms^{-1}$ or greater. The tunnel can of course run at lower speeds, but at the expense of longer experimental times and somewhat poorer flow quality.

4.2.4 Flow Simulation

Modelling the neutral boundary layer is a well established process (e.g. see Counihan, 1969 and Robins, 1979), the only matters to be decided are the choice of boundary layer depth, D, and surface roughness length, z_o. The former is directly linked to the choice of model scale. A nominally 1 m deep boundary layer was set up in the tunnel, equivalent to 200 m at 1/200 scale and 133 m at 1/133 scale. These are rather shallow by normal atmospheric standards, even for boundary layers off the sea, but greater scale reductions are ruled out by their implications regarding emission modelling. However, the project implications are minimal as the actual simulated flow conditions are included in the case specifications for numerical modelling.

The roughness length target was based on the simulation of rural conditions, implying a full scale roughness length of about 0.1 m. The tunnel floor was covered by the same array of roughness elements for all three scales of simulation. This array was designed to achieve a roughness length of between 0.5 and 1 mm in neutral conditions.

The mean velocity profile near the surface (generally assumed to mean $z/D < 0.2$) in a neutral boundary layer can be expressed by the log-law:

$$U/u^* = (1/\kappa).\ln(z/z_o)$$

where u^* is the friction velocity, κ von Karman's constant (taken to be 0.41) and z_o the roughness length. The roughness length can be evaluated by fitting the log-law to the measured mean velocity profile over the lower 20% of the boundary layer, as can the friction velocity, though this can also be measured directly (i.e. from the mean turbulent shear stress near the wall). A successful simulation should reproduce the full scale value of the non-dimensional friction velocity, u^*/U_h.

An essential feature of any satisfactory simulation is that the flow is Reynolds number independent and one measure which can be used to assess this is the roughness Reynolds number, $Re^* = u^*.z_o/\nu$. The critical, lower limit for Re^* is somewhat uncertain but a value between one and two probably applies to the sharp-edged roughness elements used in our experiments.

Simulation of stable boundary layers is considerably more complicated. The mean velocity and temperature distributions are now the log-linear profiles:

$$U/u^* = (1/\kappa).\{\ln(z/z_o) + \beta.z/L_{MO}\}$$
$$(T-T_o)/T^* = (1/\kappa).\{\ln(z/z_o) + \beta_T.z/L_{MO}\}$$

where β is a constant, L_{MO} the Monin Obukhov length scale, T_o is the surface temperature, T* the friction temperature and β_T another profile constant. We immediately see that there is another length scale to consider, defined as:

$$L_{MO} = -u^{*3}/\kappa.g.(q/T_o)$$

where q is the kinematic heat flux, u*.T*. The Monin Obukhov scale is a measure of the height at which buoyancy effects begin to dominate shear in the production of turbulence.

There are now many more parameters to be determined, the full list being: u*, T*, z_o, β and β_T, noting that u* and T* fix L_{MO}. Ideally, u* and T* should be fixed by direct measurement of the turbulent shear stress and vertical heat flux. The process then will reduce to one of determining the roughness length and the profile parameters, β and β_T. A further check on the procedure can be achieved by requiring the non-dimensional temperature fluctuation profile, $T'(z)/T^*$, to match full scale observations (e.g. Caughey et al, 1979). However, the instrumentation to pursue this in full was not available at the time of the experiments and a compromise had to be accepted. We worked from measurements of the mean velocity and temperature profiles, together with temperature fluctuation data, using the latter to fix the range for T*. We assumed a standard value of 5 for β, and then fitted the profiles to determine the remaining parameters. This is inherently a rather imprecise procedure. Recent work in the EnFlo laboratory has benefited from continuing instrumentation developments and has followed the full method described above, clearly demonstrating its advantages.

Flow and emission modelling must rest on the same basis, namely non-dimensional flux conservation achieved through similarity of:

$$L_{MO}/D,\ F_B^*,\ F_M^*$$

where D is the boundary layer depth. The ratio D/L_{MO} is actually the fundamental parameter which determines boundary layer stability and clearly must be correctly reproduced at model scale. Now, we can write:

$$D/L_{MO} = -(\kappa.g/T_o).(D.q/u^{*3})$$

which, bearing in mind that q is the kinematic heat flux per unit area, has exactly the same form as F_B^*. The basic conservation condition becomes:

$$(D.q/u^{*3})_m = (D.q/u^{*3}).$$

Now q = u*.T* and conservation of u*/U is a basic similarity requirement, so we can express the wind speed ratio by either of:

$$(U_m/U)^3 = (u^*_m/u^*)^3 = \varepsilon.(q_m/q)$$

$$(U_m/U)^2 = (u^*_m/u^*)^2 = \varepsilon.(T^*_m/T^*).$$

4.2.5 Flow and Emission Modelling in Stable Conditions

As the wind speed ratio is defined by boundary layer simulation requirements, we use the remaining similarity criteria to define the emission density ratio and then the emission speed ratio. We have:

$$(U_m/U)^2 = \varepsilon.[\{(1-\alpha_m)/(1-\alpha)\}.(\alpha/\alpha_m)^{1/2}] = \varepsilon.(T^*_m/T^*)$$

and hence:

$$(1-\alpha_m)/(1-\alpha) = (T^*_m/T^*)/(\alpha/\alpha_m)^{1/2}$$
$$(V_S/U)_m = (\alpha/\alpha_m)^{1/2}.(V_S/U)$$

4.3 The Wind Tunnel Simulations

Two boundary layer simulations were used for the experimental studies, one neutral (for cases A1, A2, B3 and C1) and the other stable (for case B5). The characteristics of the first are described in Cowan, Castro and Robins (1995) and the second in Cowan and Robins (1996c). In all cases except C1 the wind tunnel floor was covered with a uniform surface roughness pattern. Site terrain was included in C1 and the roughness elements were confined to the region upwind of the terrain model. Adding additional elements to the model surface had no effect on the observed plume behaviour.

The neutral simulation is discussed in Section 4.3.1; the main profile parameters were:

$D = 1$ m
$z_o = 0.6$ mm
$u^* = 0.050\ U_{ref}$

which for the model scales used corresponded to a shallow, neutral atmospheric boundary layer.

The properties of the stable simulation are discussed in Section 4.3.4. Two sets of profile parameters are given, one from Cowan and Robins (1996c) and the other from a more recent analysis of the same data. The results are summarised in the table below, where ΔT is the reference temperature difference, T_{ref}-T_o, and T_{ref} is the temperature at the boundary layer edge. This demonstrates that the simulation corresponded to a moderately stable atmospheric boundary layer.

Profile Property	Cowan & Robins, 1999c	This analysis
D (mm)	600	600
z_o (mm)	0.35	0.6
u^*/U_{ref}	0.029	0.020
ΔT (K)	45	45
$T^*/\Delta T$	0.014	0.020
L_{MO} (mm)	88	32
L_{MO}/D	0.15	0.05

Table 4.3
Properties of the stable boundary layer

The five wind tunnel simulations are described in some detail in the Appendix. Each description is preceded by a summary table listing the data references, the main features of the case, and the wind tunnel and equivalent full scale conditions. There then follows a description of the simulation criteria employed, the data obtained and some examples of the results. The examples are selected to demonstrate significant features from the experiments, such as the sensitivity of the observed concentrations to changes in the emission conditions. A general level of repeatability better than 10% (the design target for the equipment used) was demonstrated by all five data sets.

Case A1 deals with a passive emission and the results show how the concentration profile is displaced and distorted by the flow around the building. The four other cases deal with non-passive releases, some in more complex situations, and there is additional plume distortion and displacement as a consequence.

Emission density ratio distortion was used in all cases but A1 to ensure acceptable wind tunnel operating speeds. Case A1 concerned an ambient density emission and posed no special operational problems. The sensitivity to changes in the emission buoyancy and momentum fluxes was examined in cases A2 and B3 by running experiments at raised and lowered wind speeds, selected to change F_B^* by a factor of two. Concentrations changed by a factor between 1.2 and 1.5 in case A2, at $x/h = 5$, and by a factor between 1.1 and 1.2 in case B3, at $x/h = 2$.

B5 concerns stable boundary layer conditions and much of the discussion is given over to the application of the similarity criteria to both the flow and the emission. A dense gas release from an industrial site in complex terrain is the subject of case C1. Velocity field measurements over the site were undertaken in addition to the concentration measurements. A set of experiments was also carried out with ambient density emissions to investigate the importance of the discharge buoyancy and momentum fluxes.

4.4 Experimental Accuracy

We need to consider two separate issues, namely experimental error and simulation error. Much of the former is discussed with the individual test cases in the Appendix; the main points are brought together below:

1. The tunnel reference speed was measured with a factory calibrated anemometer, to a quoted accuracy of ±1.5%.
2. Release and calibration gases were purchased with a supplier's certificate of analysis, correct to three significant figures.
3. Gas emission rates were controlled by thermal mass flow meters and independently measured by a standard displacement flow meter with an accuracy of about ±0.25 to ±0.5%.
4. Concentration measurements were repeatable to well within ±10%.
5. Hot-wire measurements were carried out with single wire probes; the usual accuracy expected of such devices applies (e.g. see Bradshaw, 1975).
6. Temperatures were measured with cold-wire probes and thermocouples; the usual accuracy of such devices applies (e.g. ±1 K for the thermocouples). Temperatures independently measured with the two systems generally agreed to within ±0.5 K.

There are a number of matters under the general heading of simulation error. We begin by examining the assumption that all the simulated flows are Reynolds number independent and typical of the very high Reynolds numbers found at full scale. The roughness Reynolds number is the first relevant flow property to consider and for $U_{ref} = 1ms^{-1}$ we have in neutral conditions:

$$Re^* = u^*.z_o/\nu = 2$$

which indicates adequate conditions (i.e. a fully rough surface) at the flow speeds of the simulations.

Next we have the obstacle Reynolds number which based on a building height of 50 mm and $U_{ref} = 1ms^{-1}$ is:

$$Re_h = U_h.h/\nu = 1\ 800.$$

Finally, we have the source Reynolds number which, based on a diameter of 5 mm and an emission speed of 2.4 ms^{-1}, (Case 3, the most critical) is:

$$Re_d = V_S.d/\nu = 800.$$

Both Re_h and Re_d are lower than ideal. However they are probably entirely adequate in context, the first because the building is situated in a highly turbulent and strongly sheared flow region close to the ground and the second because it applies to a jet released from a the sharp-edged orifice into a cross-flow. They would not necessarily

be acceptable in other circumstances, such as an emission from a long, straight tube into a low turbulence level, uniform flow.

Next we consider the state of the simulated boundary layer itself. The neutral simulation technique has been thoroughly studied and we can confidently state the flow will be essentially the same as in a naturally developed boundary layer of the same depth over the same underlying surface. This implies that the turbulence conditions are effectively determined by a local balance between the turbulence energy production and dissipation rates. Equivalent full scale boundary layer depths were shallow in comparison with the depths expected; e.g. scaling to 200 m at 1/200 scale when the expected depth would be about 800 m. This does not create a problem as the computations were based on the appropriately scaled-up wind tunnel conditions.

Stable boundary layer simulation is a much less well established art and it is difficult to asses the quality of the simulated flow. It was with this in mind that we decided to specify the computations at model scale. Even so, only a limited picture of the flow conditions was available from the observations. An adequate specification of the flow requires direct measurement of the mean velocity and temperature profiles, together with the turbulence stresses, heat fluxes and temperature fluctuations, at several streamwise and lateral locations. We were well short of this ideal situation and had to deduce many of the parameters from the limited measurements available. Some repeated dispersion experiments were conducted, the concentration results showing somewhat more variation than in neutral conditions. However, variability was within the basic ±10% level associated with the instrumentation.

4.5 References

Bradshaw, P, 1975. An introduction to turbulence and its measurement. Pergamon Press, Oxford

Caughey, S J, Wyngaard, J C and Kaimal, J C, 1979. Turbulence in the evolving stable boundary layer. J. Atmos. Sciences, 36, 1041-1052

Counihan, J, 1969. An improved method of simulating an atmospheric boundary layer in a wind tunnel. Atmos. Environ., 3, 197-214

Cowan, I R, Robins A G and Castro, I P, 1995. Project EMU experimental data, Case A, Release I. University of Surrey, Department of Mechanical Engineering Report ME-FD/95.52

Cowan, I R and Robins A G, 1996a. Project EMU experimental data, Case A2. University of Surrey, Department of Mechanical Engineering Report ME-FD/95.54

Cowan, I R and Robins A G, 1996b. Project EMU experimental data, Case B3. University of Surrey, Department of Mechanical Engineering Report ME-FD/95.53

Cowan, I R and Robins A G, 1996c. Project EMU profile data, F2 conditions for Case B. University of Surrey, Department of Mechanical Engineering Report ME-FD/95.56

Cowan, I R and Robins A G, 1996d. Project EMU experimental data, Case B5. University of Surrey, Department of Mechanical Engineering Report ME-FD/95.55

Cowan, I R and Robins A G, 1996e. Project EMU experimental data, Case C1. University of Surrey, Department of Mechanical Engineering Report ME-FD/96.66

Heist, A, Hayden, P and Lawton, T, 1995. Instrumentation developments for EnFlo Facilities. University of Surrey, Department of Mechanical Engineering Report ME-FD/95.33

Macdonald, H F, Foster, P M, Robins, A G, and Thompson, I M G, 1988. Improved estimates of external gamma dose rates in the environs of Hinkley Point Power Station. CEGB Report RD/B/6027/R88

Obasaju, E D and Robins, A G, 1997. Simulation of pollution dispersion using small scale physical models - an assessment of scaling options. Proc. Conf. Urban Air Quality - Monitoring and Modelling, University of Hertfordshire, 11-12 July, 1996. Submitted to Environmental Monitoring and Assessment.

Robins, A G, 1979. The development and structure of simulated neutrally stable atmospheric boundary layers. J. Ind. Aero., 4, 71-100

Robins, A G, 1980. Wind tunnel modelling of buoyant emissions. Studies in Env. Sci., 8, 117-124

Robins, A G, 1996. Project EMU site and terrain data. University of Surrey, Department of Mechanical Engineering Report ME-FD/96.67

Robins, A G, 1994. Flow and dispersion around buildings in light wind conditions. Flow and Dispersion over Topography (Eds. Castro, I P and Rockliff, N J), 325-358, Clarendon Press, Oxford

Snyder, W H, 1981. Guideline for fluid modelling of atmospheric diffusion. US EPA Report EPA-600/8-81-009

APPENDIX

The Wind Tunnel Simulations

Each description is preceded by a summary table listing the data reference, the main features of the case, and the wind tunnel and equivalent full scale conditions. Descriptions of the test configurations, including building and source arrangements, are to be found in Section 3. In each case a co-ordinate system is used which has its origin at ground level immediately beneath the source.

Two boundary layer simulations were used, one neutral and the other stable. The characteristics of the first are described in Cowan, Castro and Robins (1995) and the second in Cowan and Robins (1996c).

4.3.1 Series A, Case 1

Table 4.4
A1 Case Summary

Reference	Cowan, Robins and Castro, 1995		
Model	10 m high, L-shaped building at 0° to oncoming flow		
Scale	1/200		
Atmospheric condition	neutral		
Emission	passive plume from doorway		
Property	**Model Scale**	**Full Scale**	**Units**
Height of emitting building, h	0.05	10	m
Wind speed at 10 m, U_{10}	1.0	5	ms^{-1}
Roughness length, z_o	0.6	120	mm
Boundary layer depth, D	1	200	m
Source area, A	5.10^{-4}	20	m^2
Emission density ratio, α	1	1	
Emission speed, V_S	0.2	1	ms^{-1}

Hot wire and micro-propeller anemometers were used to measure mean and turbulent velocities within the simulated boundary layer. A log-law fit to the mean velocity in the lower 20% of the layer yielded the friction velocity and roughness length. The boundary layer depth was estimated from the full set of profiles. In summary:

$u^* = 0.050\ U_{ref}$
$z_o = 0.6$ mm
D = 1.0 to 1.1 m

and D = 1 m was used as the nominal value for the simulation. Near the surface, the longitudinal turbulence intensity lay between 1.8 u* and 2.3 u*, typical of a neutral atmospheric boundary layer.

The emission was a mixture of 2.96% by volume of ethylene (C_2H_4, molecular weight 28) in a nitrogen balance. As the emission and ambient densities were equal, the only modelling criteria to be satisfied was conservation of the velocity ratio, V_S/U. At 1/200 scale the 10 m and reference wind speeds were related by:

$$U_{10}/U_{ref} = 0.55$$

so the tunnel was run at a reference speed of 1.8 ms^{-1}.

Mean concentration measurements were made at the following stations:

$$x/h = 0.5, 1, 2, 5, 10.$$

Lateral profiles were obtained at a number of heights at each location, thus mapping the concentration field in planes of constant x. By way of illustration, Figure 4.2 shows results at x/h = 1; profiles of the non-dimensionalised volume concentration, C*, are plotted as functions of y/h at z/h = 0.16, 0.36, 0.68, 1.02, 1.48 and 2.0, with C* defined by:

$$C^* = C.U_h.h^2/Q$$

as described in Section 4.1. Some repeat runs are included which show repeatability well within the nominal level of 10% for the measurement techniques used. The concentration profiles are non-Gaussian with properties (e.g. the lateral position of maximum concentration) which vary with height. Clearly, part of the plume was forced to pass around the building before being carried downwind, and part passed over the roof.

Cowan, Robins and Castro (1995) lists the full concentration data set. Tabulations of the boundary layer profiles of mean velocity and longitudinal turbulence are also included.

4.3.2 Series A, Case 2

Table 4.5 **A2 Case Summary**			
Reference	Cowan and Robins, 1996a		
Model	10 m high, L-shaped building at 45° to oncoming flow		
Scale	1/133		
Atmospheric condition	neutral		
Emission	buoyant jet from 1 m diameter hole		
Property	**Model Scale**	**Full Scale**	**Units**
Height of emitting building, h	0.075	10	m
Wind speed at 10 m, U_{10}	0.77	5	ms^{-1}
Roughness length, z_o	0.6	80	mm
Boundary layer depth, D	1	133	m
Source diameter, d	0.0075	1.0	m
Emission density ratio, α	0.18	0.55	
Emission speed, V_S	6.75	25.0	ms^{-1}

Density distortion was essential to maintain a reasonable wind tunnel operating speed. This was achieved by using a mixture of 5.07% by volume of ethylene in a helium balance. Simulation was then based on similarity of the non-dimensional emission momentum and buoyancy fluxes with a density ratio distortion of 3.1 (0.55/0.18). At 1/133 scale, the relationship between the 10 m and reference speeds was:

$$U_{10}/U_{ref} = 0.60$$

so the tunnel was run at a reference speed of 1.3 ms^{-1}.

Mean concentration measurements were made at the following stations:

$$x/h = 2, 5, 10, 20.$$

Lateral profiles were obtained at a number of heights at each location, thus mapping the concentration field in planes of constant x. By way of illustration, Figure 4.3 shows results at x/h = 5; profiles of the non-dimensionalised volume concentration, C*, are plotted as functions of y/h at z/h = 0.49 and 1.96. Again we see the concentration profiles are non-Gaussian and that part of the plume was forced to pass around the building before being carried downwind, and part passed over the roof.

In this problem, the non-dimensional emitted buoyancy and momentum fluxes are:

$$F_B^* = 0.069; \quad F_M^* = 0.11$$

which implies that both buoyancy and momentum effects are important, but that the plume is unlikely to lift from the ground (e.g. see Robins, 1994). The measurements confirm this picture.

Runs were also carried out with the tunnel reference speed raised to 1.64 ms^{-1} and lowered to 1.03 ms^{-1}, thus changing F_B* by a factor of two and, as a consequence, F_M* by a factor of 1.59. Figure 4.3 includes results from these runs and we see that concentrations changed by a factor of approximately 1.5 at z/h = 0.49 and 1.2 at z/h = 1.96. At the lower level concentrations are greatest at the higher wind speed, whilst at the upper level they are greatest at the lower wind speed. Buoyancy effects are most significant at the low wind speed and least significant at the high wind speed and the resulting change in plume height accounts for the observed change in concentration levels. These observations provide a sensitivity test by which to judge differences between predictions and measurements. Some repeat runs were carried out and again these showed repeatability well within the nominal level of 10% for the measurement techniques used.

Cowan and Robins (1996a) lists the full concentration data set. Tabulations of the boundary layer characteristics are to be found in Cowan, Robins and Castro (1995).

4.3.3 Series B, Case 3

Table 4.6
Case Summary B3

Reference	Cowan and Robins, 1996b		
Model	10 m high, L-shaped at 75˚ to oncoming flow plus 20 m high downwind, slab-shaped building		
Scale	1/200		
Atmospheric condition	neutral		
Emission	dense jet from 1 m diameter hole		
Property	**Model Scale**	**Full Scale**	**Units**
Height of emitting building, h	0.05	10	m
Wind speed at 10 m, U10	0.72	5	ms^{-1}
Roughness length, zo	0.6	120	mm
Boundary layer depth, D	1	200	m
Source diameter, d	0.005	1.0	m
Emission density ratio, α	2.82	1.30	
Emission speed, V_S	2.44	25.0	ms^{-1}

Density distortion was essential to maintain a reasonable wind tunnel operating speed. This was achieved by using a mixture of 3.51% by volume of ethylene in a krypton balance. Simulation was then based on similarity of the non-dimensional emission momentum and buoyancy fluxes with a density ratio distortion of 2.2 (2.82/1.30). At 1/200 scale the relationship between the 10 m and reference speeds was:

$U_{10}/U_{ref} = 0.55$

so the tunnel was run at a reference speed of 1.3 ms^{-1}.

Mean concentration measurements were made at the following stations:

x/h = 1, 2, 5, 10, 20.

Lateral profiles were obtained at a number of heights at each location, thus mapping the concentration field in planes of constant x. By way of illustration, Figure 4.4 shows results at x/h = 2; profiles of the non-dimensionalised volume concentration, C*, are plotted as functions of y/h at z/h = 0.12 and 1.4. Again we see the concentration profiles are non-Gaussian. However, in this case most of the plume passed around the building before being carried downwind, and only a small fraction passed over the roof.

In this problem, the non-dimensional emitted buoyancy and momentum fluxes are:

$F_B^* = -0.046$; $F_M^* = 0.25$,

the minus sign denoting a heavier than air emission. These values imply that both buoyancy and momentum effects are important, but that the plume is unlikely to be dominated by gravitational effects (e.g. see Robins, 1994). The measurements confirm this picture.

Runs were also carried out with the tunnel reference speed raised to 1.64 ms^{-1} and lowered to 1.03 ms^{-1}, thus changing F_B^* by a factor of two and, as a consequence, F_M^* by a factor of 1.59. Figure 4.4 includes results from these runs and we see that concentrations changed by a factor of approximately 1.1 to 1.2, less than in the previous case. At z/h = 0.12 concentrations are greatest at the lower wind speed, whilst at z/h = 1.04 they are greatest at the higher wind speed. Buoyancy effects are most significant at the low wind speed and least significant at the high wind speed and the resulting change in plume height accounts for the observed change in concentration levels. These observations provide a sensitivity test by which to judge differences between the predictions and measurements. Some repeat runs were carried out and again these showed repeatability well within the nominal level of 10% for the measurement techniques used.

Cowan and Robins (1996b) lists the full concentration data set. Tabulations of the boundary layer characteristics are to be found in Cowan, Robins and Castro (1995).

4.3.4 Series B, Case 5

Table 4.7 **Case Summary B5**			
References	Cowan and Robins, 1996c, d		
Model	10 m high, L-shaped at 45˚ to oncoming flow		
Scale	1/133		
Atmospheric condition	stable		
Emission	buoyant jet from 1 m diameter hole		
Property	**Model Scale**	**Full Scale**	**Units**
Height of emitting building, h	0.075	10	m
Wind speed at 10 m, U_{10}	0.72	3.0	ms^{-1}
Roughness length, z_o	0.35	40	mm
Boundary layer depth, D	1	133	m
Monin Obukhov scale, L_{MO}	0.077	10	m
Source diameter, d	0.0075	1.0	m
Emission density ratio, α	0.18	0.81	
Emission speed, V_S	13.7	25.0	ms^{-1}

The properties of the simulated stable boundary layer are described in Cowan and Robins (1996c) . The simulation was generated by running the tunnel in the following condition:

Reference speed, U_{ref}: 1 ms^{-1},
Bulk flow temperature, T_{ref}: 60 ˚C,
Surface temperature, T_o: 15 ˚C.

Profile measurements of mean velocity, mean temperature and temperature fluctuations were made with a micro-propeller anemometer, thermocouples and a cold-wire anemometer. The analysis proceeded along the lines discussed in Section 4.2.4. The mean velocity and temperature data were fitted to log-linear profiles, subject to correct simulation of atmospheric data for the non-dimensional temperature fluctuation profile, $T'(z)/T^*$.

The data has been re-analysed since the publication of Cowan and Robins (1996c) using the log-linear profile given in Section 4.2.4 . Previously a form including the turbulent Prandtl number, σ_τ, had been applied; namely:

$$U/u^* = (1/\kappa).\{\ln(z/z_o) + \beta.z/L_{MO}\}$$
$$(T-T_o)/T^* = (\sigma_\tau/\kappa).\{\ln(z/z_o) + \beta_T.z/\sigma_\tau.L_{MO}\}.$$

The profile parameters from the two analyses are listed below, in Table 4.8, where ΔT is the reference temperature difference, T_{ref}-T_o.

Profile Property	**Cowan & Robins, 1996c**	**This analysis**
D, mm	600	600
σ_τ	0.74	1.0
z_o, mm	0.35	0.6
U_{ref}, ms^{-1}	1.0	1.0
u*, ms^{-1}	0.029	0.020
ΔT, K	45	45
T*, K	0.65	0.90
u*.T*, Kms^{-1}	0.019	0.018
β	5	5
β_T	21	8
L_{MO}, mm	88	32
L_{MO}/D	0.15	0.05

Table 4.8
Properties of the stable boundary layer

Figure 4.5a compares the tabulated data (Cowan and Robins, 1996c) with the log-linear profiles, and 4.5b the non-dimensional temperature fluctuation profile with the field data of Caughey et al (1979), using the new set of profile parameters. The log-linear profiles are only valid up to $z/L_{MO} \approx 1$, so the agreement is really quite good with the log-linear regime extending to about $z/L_{MO} = 2$ in velocity and $z/L_{MO} = 1$ in temperature. The original set of parameters provides a slightly inferior fit to the data. Interestingly, in both cases the kinematic heat flux, u*.T*, was virtually the same. Both analyses indicate that the simulation was equivalent to a moderately stable atmospheric boundary layer; i.e. with $D/L_{MO} = O(10)$.

The experimental design procedure for this problem can be summarised by the following sequence of events:

1. define the scale ratio, ε, and hence h and L_{MO},
2. estimate the appropriate kinematic surface heat flux, q, at full scale,
3. select a tunnel speed and then calculate the equivalent wind speed,
4. iterate to achieve a consistent set of full scale conditions
5. calculate the density ratio, α, equivalent to the model value, α_m,
6. calculate the model emission speed and volume flow rate.

Before proceeding further we return to the similarity equations derived in Sections 4.2.4 and 4.2.5 and repeated below:

$$(U_m/U)^3 = (u^*_m/u^*)^3 = \varepsilon.(q_m/q)$$
$$(U_m/U)^2 = (u^*_m/u^*)^2 = \varepsilon.(T^*_m/T^*)$$

$$(1-\alpha_m)/(1-\alpha) = (T^*_m/T^*)/(\alpha/\alpha_m)^{1/2}$$
$$(V_S/U)_m = (\alpha/\alpha_m)^{1/2}.(V_S/U)$$

These results show that if q_m and q are fixed then so is U_m/U, u^*_m/u (and hence T^*_m/T^*), α_m/α and V_{Sm}/V_S. This is a consequence of basing all the similarity criteria on the conservation of the non-dimensional fluxes. We need only describe the details of the design procedure for one of the sets of flow properties listed in Table 4.8. This is done below for the Cowan and Robins (1996c) set; actually, we use a matched set (i.e. $q = u^*.T^*$) rather than the range means quoted in Cowan and Robins.

(1) We selected the scale ratio as $\varepsilon = 1/133$ to ensure that L_{MO} was of the same order as the building height, h. Clearly, any value of ε in the range from about 1/133 to 1/330 would have been plausible but we chose the former value to ensure that a low full scale wind speed was simulated (i.e. noting that $U/U_m = \varepsilon^{-1/3}.(q_m/q)^{-1/3}$). Equivalent model and full scale values of h and L_{MO} are tabulated below.

Model scale:
L_{MO} = 88 mm; h = 75 mm
Full scale:
L_{MO} = 12 m; h = 10 m

(2) Next we took the downward heat flux, S, in the moderately stable atmospheric boundary layer to be of order 10 Wm^{-2}, so that $q = S/\rho.Cp \approx 8.04.10^{-3}$ Kms^{-1}.

(3) The wind tunnel reference speed of 1 ms^{-1} was used together with the information in (1) and the scale relations:

$$U_m/U = \varepsilon^{1/3}.(q_m/q)^{1/3}$$
$$T^*_m/T^* = (1/\varepsilon).(U_m/U)^2$$

to calculate the roof level wind speed and hence the friction velocity and friction temperature at full scale. The Monin Obukhov length scale is then evaluated to check the overall calculation.

Model scale: $U_h/U_{ref} = 0.70$; $u^*/U_h = 0.041$
Scaling ratios: $U_m/U = 0.29$; $T^*_m/T^* = 9.1$
Full scale: $U_h = U_{10} = 2.7$ ms^{-1}; $u^* = 0.11$ ms^{-1}
$T^* = 0.071$ K; $q = u^*.T^* = 7.8.10^{-3}$ Kms^{-1}; $L_{MO} = 12.2$ m

(4) No iteration was needed as the calculated kinematic heat flux, q, was close enough to the target value set in (2) above.

(5) The release into the wind tunnel was a mixture of 5.07% by volume of ethylene in a helium balance, so $\alpha_m = 0.18$. We then solved the emission density relationship of Section 4.2.5 to find the full scale equivalent density ratios, α, to be 0.81.

(6) The model scale emission speed and volume flow rates were then calculated as:

Full scale: $V_S/U_h = 9.3$
Model scale: $V_S = 13.8\ ms^{-1}$; $Q = 6.1.10^{-4}\ m^3s^{-1}$

Mean concentration measurements were made at the following stations:

x/h = 2, 5, 10, 20.

Lateral profiles were obtained at a number of heights at each location, thus mapping the concentration field in planes of constant x. By way of illustration, Figure 4.6 shows contours of the non-dimensionalised volume concentration, C*, at the four stations. The plume centre has been displaced due to the flow around the building and also the emission momentum and buoyancy.

The non-dimensional emitted buoyancy and momentum fluxes are:

$F_B^* = 0.19$; $F_M^* = 0.54$

which confirms that both buoyancy and momentum effects are important, though again the plume is unlikely to lift-off from the ground (e.g. see Robins, 1994). The importance of boundary layer stability is measured by the ratio of the Monin Obukhov length scale and the building height. We have:

$L_{MO}/h \approx 1$

indicating that stability is indeed important, though not dominant.

Cowan and Robins (1996d) lists the full concentration data set. Tabulations and plots of the boundary layer characteristics are to be found in Cowan and Robins (1996c).

4.3.5 Series C, Case 1

The model was constructed from the digital terrain data and building drawings supplied to all participants (Robins, 1996). The terrain model was manufactured from polyurethane foam, in 1 m square panels which were milled using a 5 mm (1.25 m at full scale) cutting interval. The model was left in its 'stepped' form as this provided a certain amount of surface roughness. It was installed in the wind tunnel with the standard roughness array upstream; the approach flow being the 1 m deep neutral boundary layer described in Cowan, Castro and Robins (1995). The upstream tunnel floor represented sea level. Some exploratory dispersion experiments showed that additional roughness mounted on the model had no significant impact on plume behaviour, so the basic model plus site buildings was used for the bulk of the experimental work.

Table 4.9 **Case Summary C1**			
Reference	Cowan and Robins, 1996e		
Model	complex industrial site, with terrain; wind off the sea		
Scale	1/250		
Atmospheric condition	neutral		
Emission	dense jet from 1.74 m diameter hole		
Property	**Model Scale**	**Full Scale**	**Units**
[1]Height of emitting building, h	0.04	10	m
[2]Wind speed at 10 m, U_{10}	0.90	5	ms^{-1}
[2]Roughness length, z_o	0.6	150	mm
[2]Boundary layer depth, D	1	250	m
Source diameter, d	0.007	1.74	m
Emission density ratio, α	2.82	1.14	
Emission speed, V_S	7.98	70.0	ms^{-1}
(1) nominal value (2) refers to approach flow conditions over the sea			

Density distortion was essential to maintain a reasonable wind tunnel operating speed. This was achieved by using a mixture of 3.51% by volume of ethylene in a krypton balance. Simulation was then based on similarity of the non-dimensional emission momentum and buoyancy fluxes with a density ratio distortion of 2.5 (2.82/1.14). The relationship between the 10 m and reference speeds at 1/250 scale was:

$$U_{10}/U_{ref} = 0.53$$

so the tunnel was run at a reference speed of 1.7 ms^{-1}. Some additional experiments with an ambient density emission were used to quantify the importance of local flow conditions around the emitting building and the relative importance of the buoyancy and momentum fluxes from the source.

Mean concentration measurements were made at a number of stations between x/h = 5 and 68, the most detailed results being obtained at:

$$x/h = 11, 30, 45, 68.$$

Lateral and vertical mean concentration profiles were obtained at each of these four locations. At other stations only limited lateral profiles at ground level were measured, sufficient to determine plume centre-line conditions. A number of vertical profiles of mean velocity and longitudinal turbulence were also obtained. These were sufficient to define the modified flow over the terrain, upwind and downwind from the emitting building, both with and without an emission (which was actually an ambient density discharge with the same momentum flux as the dense gas release).

Figure 4.7a shows the emitting building and the source arrangement, and Figure 4.7b the whole site. By way of illustration, Figure 4.8 plots the non-dimensional plume centre-line, ground level concentration and its lateral location as a function of distance downwind from the source. In addition to the dense gas jet (code DJ in the figure) are results for ambient density jets (code NJ) of emission velocity ratios: V_S/U_h = 0.8, 1.4, 7.5 and 15.2. The latter possesses the same source momentum flux as the dense gas jet. We see however that the dense plume is somewhat less diluted and is displaced further across the flow. Vertical profiles of concentration showed it also to be somewhat shallower than the air jet. One further noteworthy point is demonstrated by the two lowest momentum flux discharges. They follow virtually the same path, their displacement being entirely due to mean flow deflection by the site buildings and terrain, rather than their initial momentum.

In this problem, the non-dimensional emitted buoyancy and momentum fluxes (for the dense gas jet) are:

$$F_B^* = -0.18; \quad F_M^* = 5.3$$

which implies that momentum effects are likely to dominate, though buoyancy is not entirely negligible (e.g. see Robins, 1994). The measurements confirm this picture.

Some repeat runs were carried out and again these showed repeatability well within the nominal level of 10% for the measurement techniques used. These repeatability studies are summarised in Cowan and Robins (1996e). Roughening the model surface to simulate built-up areas had no effect on plume dispersion behaviour.

The flow field measurements, also reported in Cowan and Robins (1996e) reveal a very strong perturbation due to the jet. A wake region with reduced mean velocity and increased turbulence is generated by the cross-flow over the jet.

Cowan and Robins (1996e) lists the full concentration data set. Tabulations of the boundary layer characteristics are to be found in Cowan, Robins and Castro (1995).

Figures

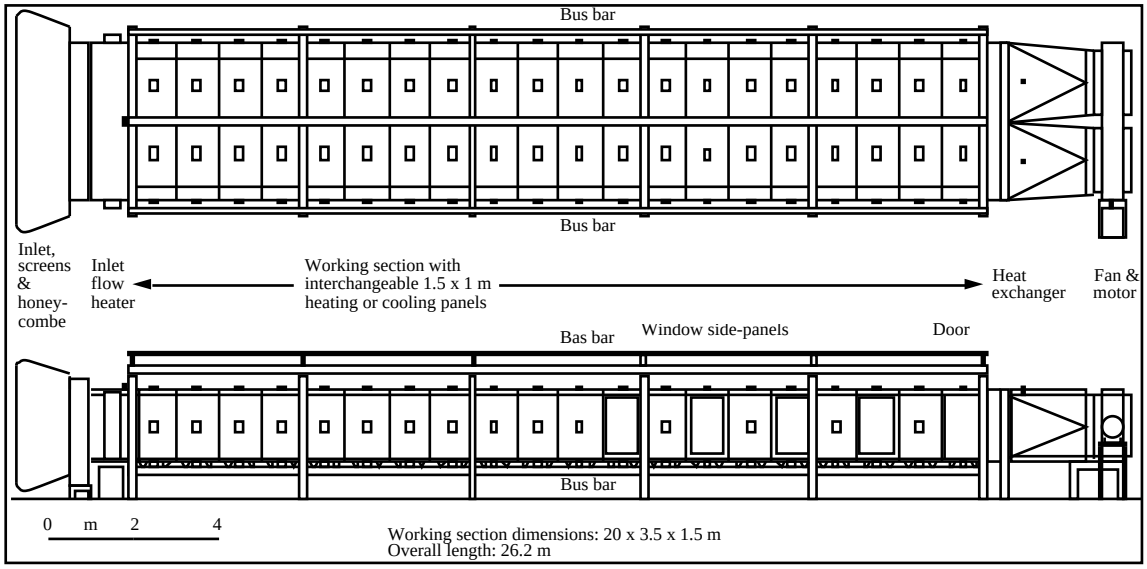


Figure 4.1a. The EnFlo stratified flow wind tunnel.

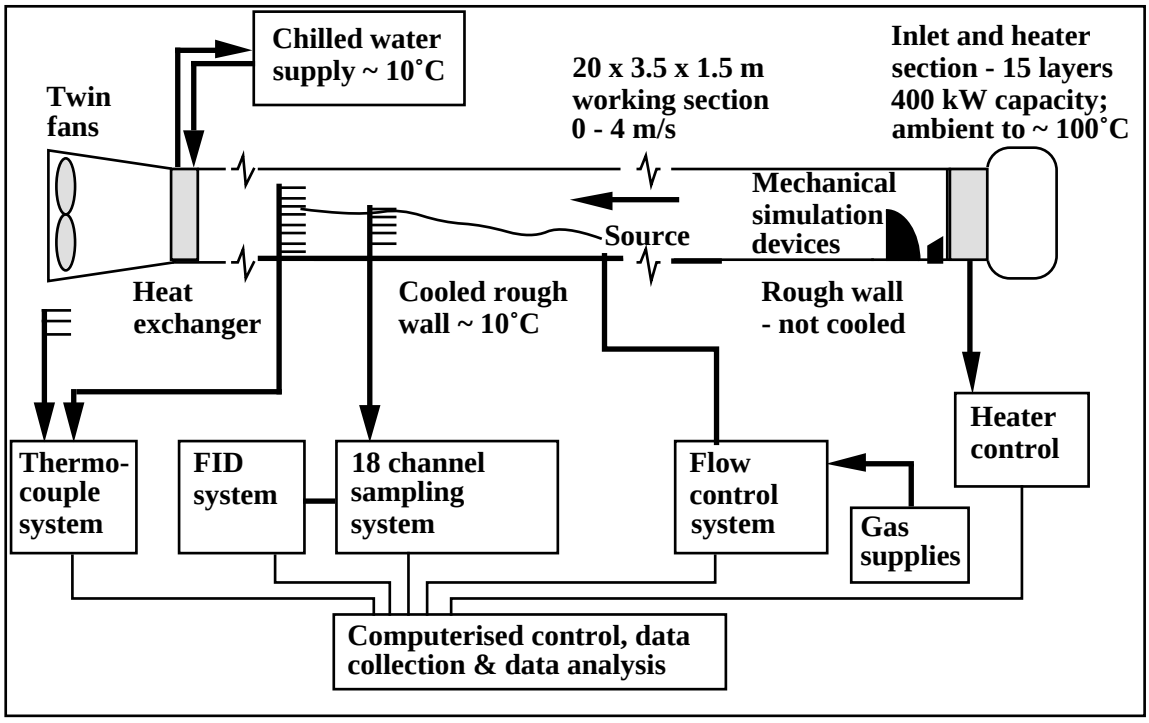


Figure 4.1b. Configuration of the EnFlo wind tunnel and auxiliary equipment when used to simulate a stable boundary layer.

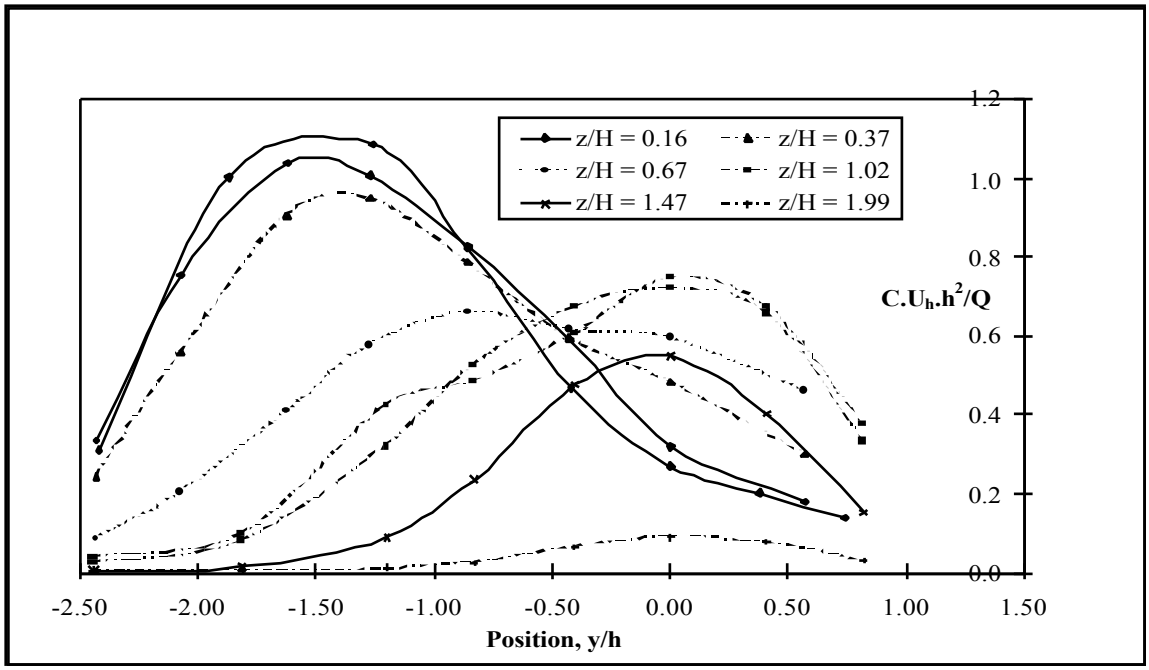


Figure 4.2. Case A1: Concentration profiles at x/h = 1

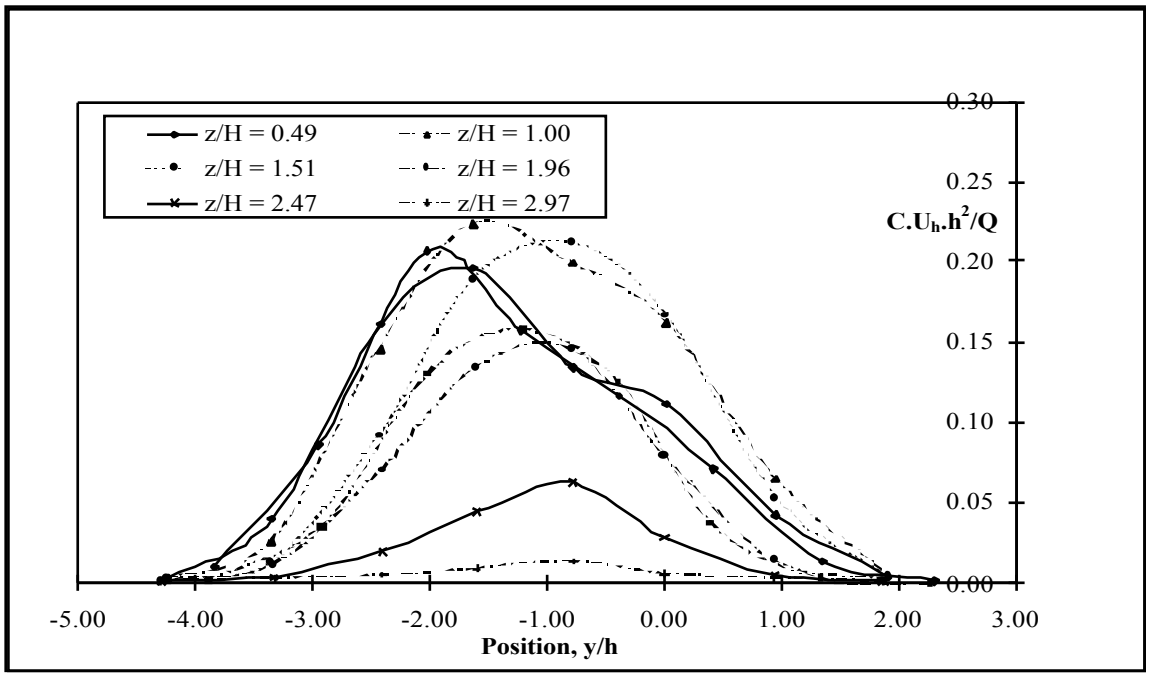


Figure 4.3. Case A2: Concentration profiles at x/h = 5

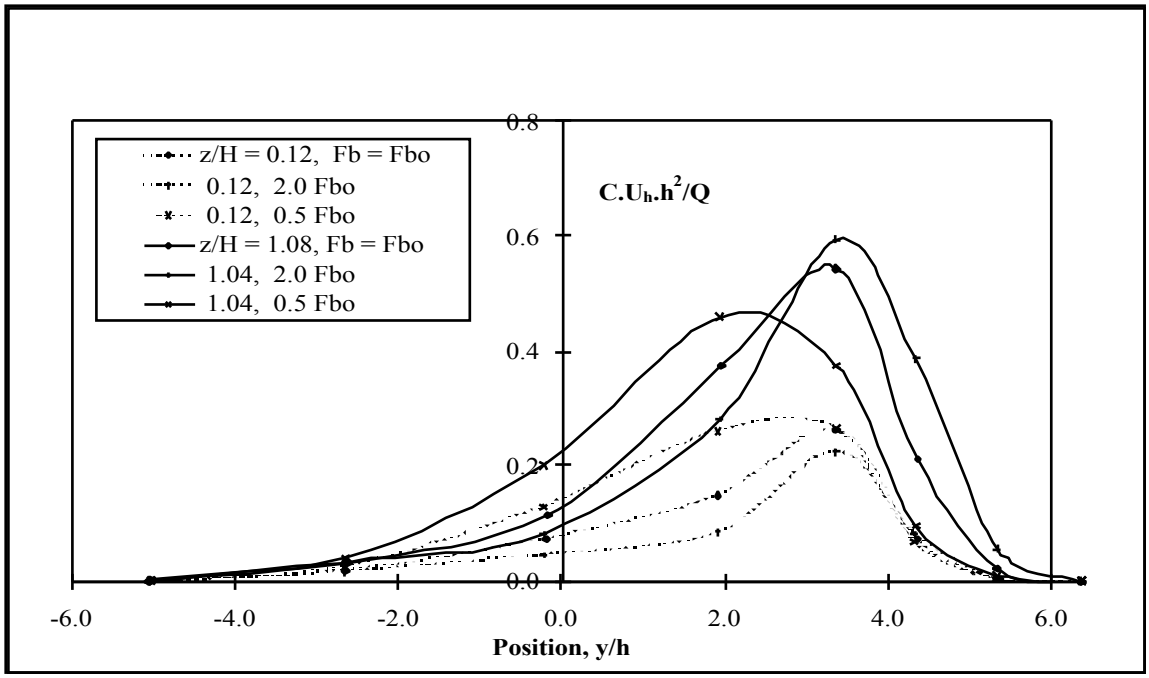


Figure 4.4. Case B3: Concentration profiles at x/h = 2

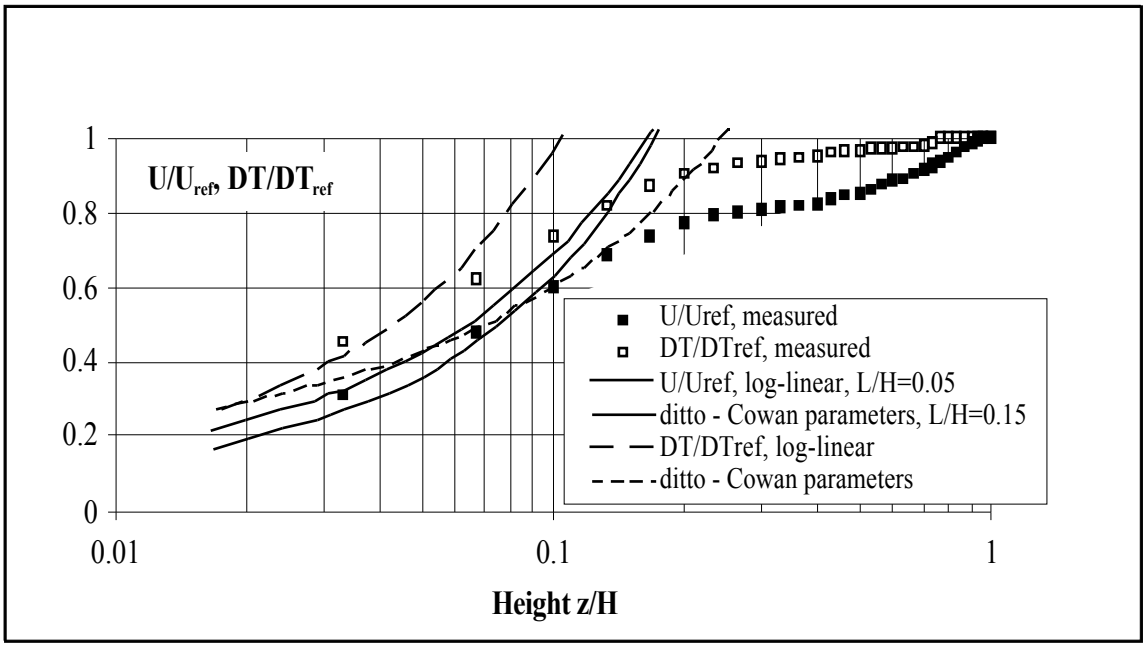


Figure 4.5a. Mean velocity and temperature distributions in the simulated stable boundary layer compared with log-linear profiles.

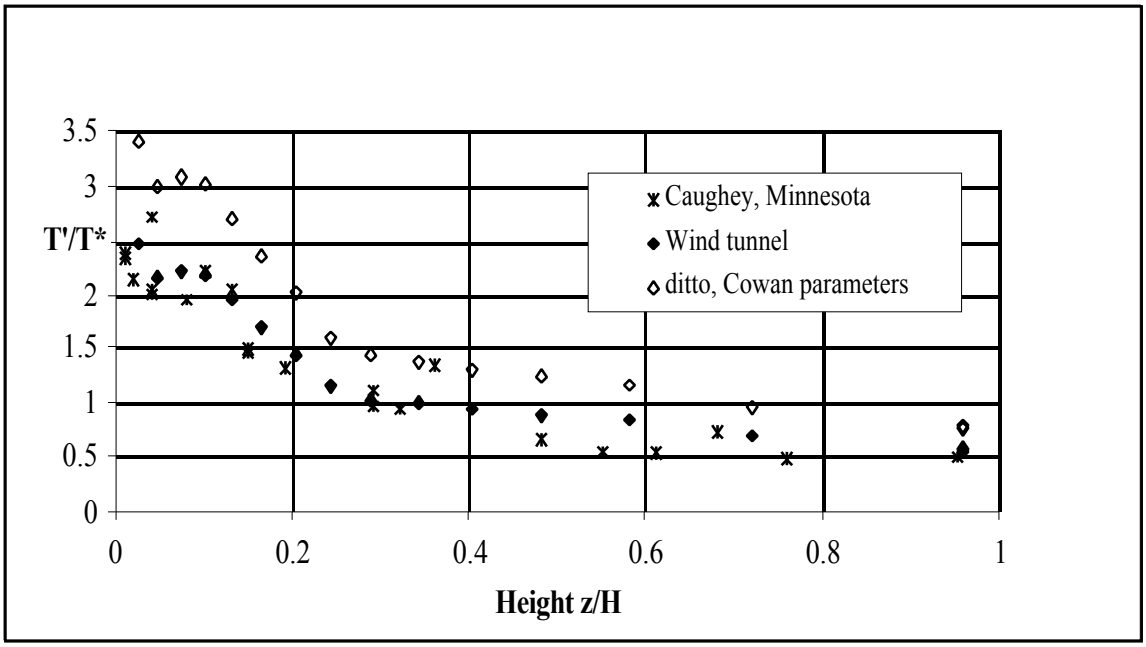


Figure 4.5b. Temperature fluctuation profiles in the simulated stable boundary layer and in the atmosphere.

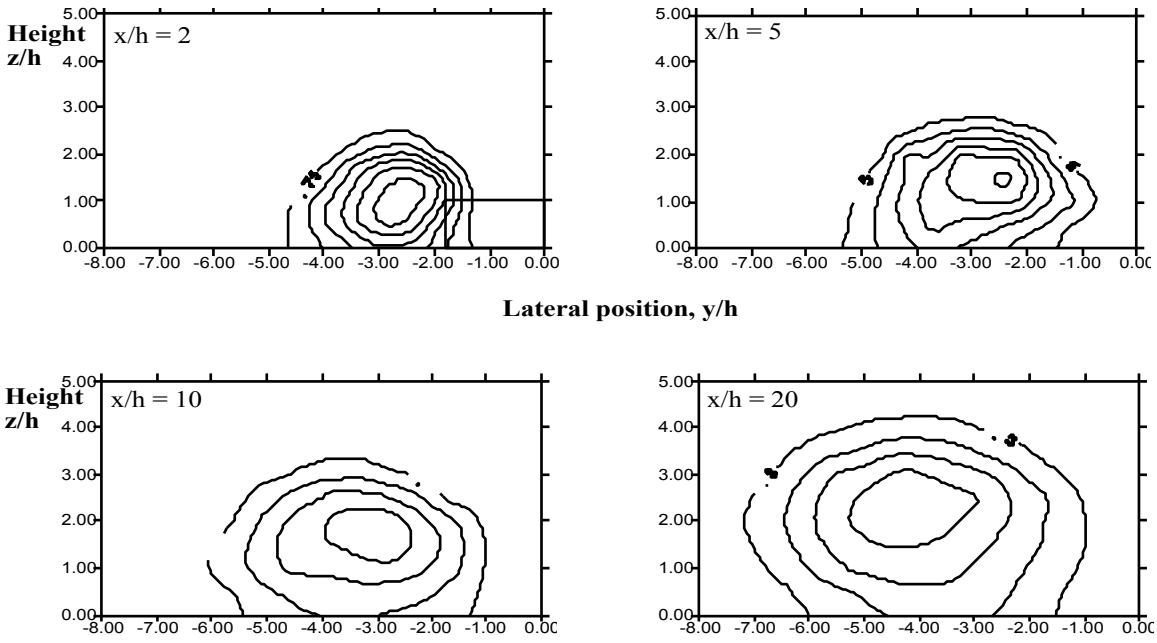


Figure 4.6. Case B5: Concentration contours at x/h = 2, 5, 10 and 20.

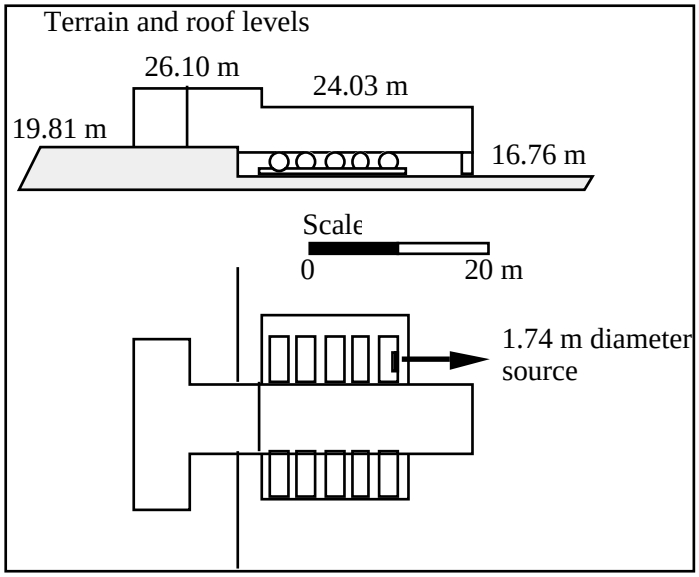


Figure 4.7a. Case C1: Source arrangement.



Figure 4.7b. Case C1: Site and terrain map.

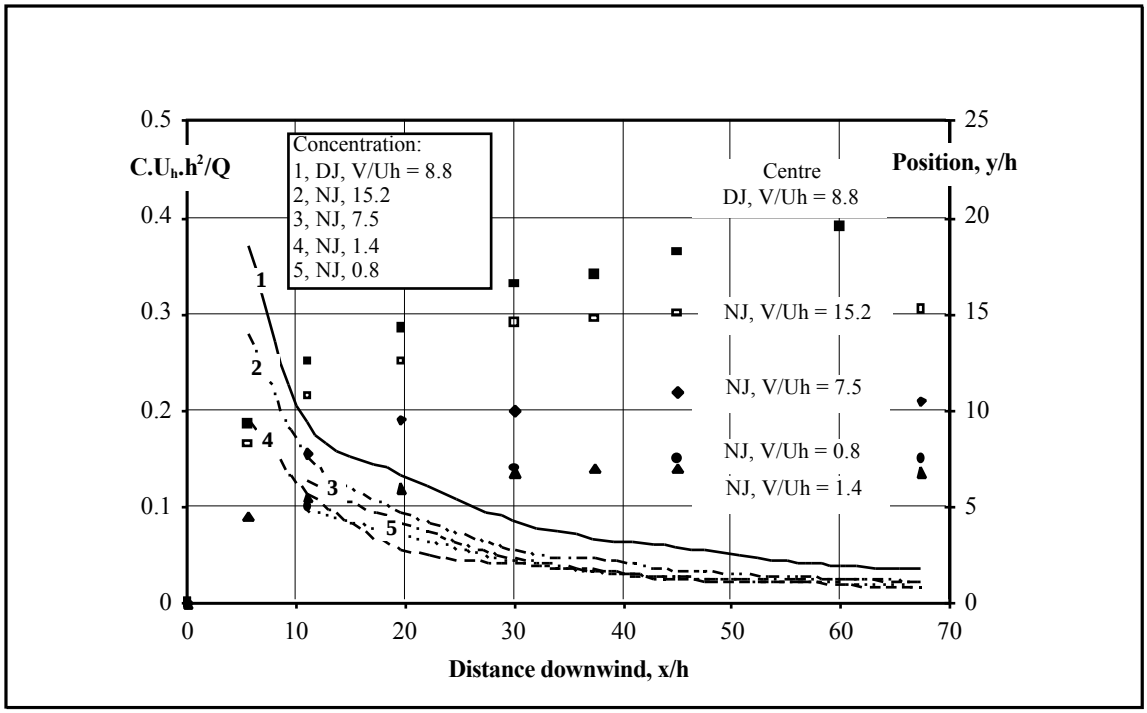


Figure 4.8. Case C1: Plume centre-line ground level concentrations and lateral displacement as a function of distance.